Su *et al. J Mater Inf* 2023;3:14
DOI: 10.20517/jmi.2023.12

Journal of Materials Informatics

Research Article

Open Access

Composition- and temperature-dependence of β to ω phase transformation in Ti-Nb alloys

Yunting Su, Chuanxin Liang, Dong Wang*

Center of Microstructure Science, Frontier Institute of Science and Technology, State Key Laboratory for Mechanical Behavior of Materials, Xi'an Jiaotong University, Xi'an 710054, Shaanxi, China.

***Correspondence to:** Prof. Dong Wang, Center of Microstructure Science, Frontier Institute of Science and Technology, State Key Laboratory for Mechanical Behavior of Materials, Xi'an Jiaotong University, 99 Yanxiang Road, Xi'an 710054, Shaanxi, China. E-mail: wang_dong1223@xjtu.edu.cnf

How to cite this article: Su Y, Liang C, Wang D. Composition- and temperature-dependence of β to ω phase transformation in Ti-Nb alloys. *J Mater Inf* 2023;3:xx. https://dx.doi.org/10.20517/jmi.2023.12

Received: 30 Mar 2023 **First Decision:** 24 May 2023 **Revised:** 12 Jun 2023 **Accepted:** 27 Jun 2023 **Published:** 11 Jul 2023

Academic Editor: Xingjun Liu **Copy Editor:** Dong-Li Li **Production Editor:** Dong-Li Li

Abstract

ω phases have shown great effects on the superelasticity and modulus of metastable β-Ti alloys. In this study, the microstructure evolution during cooling and aging for β → ω phase transformation is investigated by integrating a thermodynamic database with phase field simulations. Our CALPHAD calculations based on an available thermodynamic database give the Gibbs energies of metastable β (Nb-lean β_1 + Nb-rich β_2 produced via spinodal decomposition) and ω phases in Ti-Nb. Informed by the results, our phase field simulations show that the formation mechanisms of ω exhibit dependence on the composition and temperature. The ω can form in Ti-26 at.% Nb without the assistance of spinodal decomposition. Further analysis shows that the precursory spinodal decomposition in the β phase occurs in Ti-50 at.% Nb, and could induce geometrically confined ω. The novel transformation pathway could create unique morphology of ω. This study could elucidate new insights into the ω phase transformation in Ti-Nb alloys and metastable β-Ti alloys having spinodal decomposition.

Keywords: Omega phase, Ti-Nb, microstructural evolution, spinodal decomposition, phase field simulation

INTRODUCTION

Ti-Nb-based ferroelastic materials have attracted considerable attention for use in biomedical applications due to their superelasticity, low modulus, high strength, good ductility, and excellent biocompatibility[1-3].

The superelasticity can be obtained at room temperature and is generally associated with a martensitic transformation from β (bcc) to α" (orthorhombic)[4,5]. However, a metastable ω phase (hexagonal) is also easily formed in the β matrix[5-9] and exhibits higher modulus than the β and α" phases[10,11]; thus, the ω phase increases the modulus of the Ti-Nb-based ferroelastic systems[11,12]. Fine and dense ω particles also increase the critical stress for slip deformation and thus increase the recovery strain of ferroelastic materials[5].

Thermally, the β → ω transformation has been classified into athermal and isothermal types[10]. The former takes place via quenching from high temperature (β-phase field) to lower temperature, such as room temperature, whereas the latter is by isothermal aging or upon slow cooling, such as air cooling and furnace cooling. Athermal ω is very fine, normally less than 5 nm, with an ellipsoidal shape[13-15]. It generally retains the same composition as the parent β matrix, takes place via the diffusionless, displacive mechanism[9], and has been detected in solution-treated Ti-(21~27) at.% Nb alloys[16,17]. Athermal results from the reduced stability of a β phase through the movement of the $\{222\}_\beta$ planes via atomic shuffle, which movement causes a partial collapse of $\{111\}_\beta$ planes[1,18]. Isothermal ω has a size of about several to several hundreds of nanometers[5,13,19], with an ellipsoidal shape in Ti-Nb-based alloys because of the low lattice misfit[20]. A complete displacive collapse of $\{111\}_\beta$ planes can be gradually accomplished with increasing aging time as the rejection of -stabilizing elements from ω[21,22]. High-density fine isothermal ω precipitates have been found in Ti-26 at.% Nb alloy upon aging at 573 K and 673 K for 1 h[5], showing a decreased volume fraction with increasing aging temperature. As the aging time increases to 10 h, the coarsening of the ω particles formed after 673 K aging is much clearer than that formed after 573 K aging. But the nature of the structural difference observed in Ti-26 at.% Nb after aging at different temperatures is still unclear.

Moreover, isothermal ω is generally thought to form via diffusion-dominated mechanisms. The coexistence of isothermal ω and spinodal decomposition has been found in many metastable β-Ti alloys, such as Ti-9 at.% Mo[18], Ti-23Nb-2O (at.%)[14], Ti-24.2Nb-3.96Zr-8.1Sn (wt.%, Ti2448)[23,24], Ti-(21, 27) at.% V[25], and Ti-6Cr-5Mo-5V-4Al (wt.%, Ti-6554)[26], by using advanced characterization techniques of aberration-corrected high-resolution transmission electron microscopy (HRTEM) and three-dimensional atom probe tomography (APT). Miscibility gaps have been reported in the metastable β-Ti alloys of Ti-Nb, Ti-Mo, and Ti-V systems[27] that exhibited nanosized ω, and the spinodal decomposition can change local composition continuously at fine scales[4]. Previous work has also shown that the shape of isothermal ω changes from an ellipsoid shape to an elongated rod shape with increasing oxygen in Ti-20Nb-(0.1~4.8) O (at.%) alloys after aging at 723 K[19]. However, the relationship between the spinodal decomposition of β and the formation of ω is still not fully understood, and two different insights have been reported. The first is a coupled diffusional-displacive mechanism[18]. The gradually increased collapse degree of $\{111\}_\beta$ planes and rejection of Mo element from ω were simultaneously detected in aged Ti-9 at.% Mo alloy after aging at 748 K. However, it is experimentally difficult to verify whether the Mo partitioning is caused by the growth of isothermal ω or the spinodal decomposition of β. Additionally, structural reconstruction assisted by nanoscale spinodal decomposition was proposed in Ti-6554[26] using the selected area diffraction pattern (SADP) and APT after aging at 573 K. There are huge differences of alloy compositions and aging conditions for the above two cases; therefore, the mechanism of β → isothermal ω still requires classification. However, few studies have shown the effect of alloy composition[12,19] and aging temperature[5] on the spinodal decomposition and isothermal ω transformation in an alloy system, which effect on the microstructural evolution of ω is still not well understood.

In this study, using simple binary Ti-Nb alloys as examples, we study the phase transformations from β to athermal and isothermal ω by integrating CALPHAD modeling and phase field simulations. Two alloy

compositions of Ti-26 at.% Nb and Ti-50 at.% Nb are selected, and the conditions upon water quenching from 1,173 to 300 K and isothermal aging at 573 K and 673 K to 256 h have been considered. The simulation results show homogeneous nucleation in as-quenched and aged Ti-26 at.% Nb. Further analysis reveals that nanoscale concentration modulation preferentially occurs via spinodal decomposition upon cooling and isothermal aging in Ti-50 at.%Nb, which amplitude and wavelength change as a function of aging time and temperature, and has a great geometrical constraint on the subsequent microstructural evolution of the athermal and isothermal ω particles.

MATERIALS AND METHODS

Phase diagram and Gibbs energy

The system considered is a binary Ti-Nb single crystal. The calculated Ti-Nb phase diagram has shown a ω + β two-phase region, as shown in Figure 1. The bulk chemical energies of homogeneous β and ω phases at different temperatures are obtained from the literature[27] and can be formulated as follows:

$$G_{\phi} = c\,{}^{0}G_{Nb}^{\phi} + (1-c)\,{}^{0}G_{Ti}^{\phi} + RT\,[c\ln c + (1-c)\ln(1-c)] + c(1-c)I^{\phi} \quad (1)$$

where ϕ represents the β or ω phase, c is the mole fractions of Nb, R is the gas constant, and T is the absolute temperature. ${}^{0}G_{Nb}^{\phi}$ and ${}^{0}G_{Ti}^{\phi}$ are the Gibbs energies of pure elements Nb and Ti in the ϕ state based on the *SGTE* database. I^{ϕ} is the regular solution parameter having I^{β} = 13,075 J/mol and I = 2,510 J/mol. For numerical calculation in the following phase field simulations, the Gibbs energies of the metastable β and ω phases can be fitted as a function of Nb concentration and temperature:

$$G_{\omega,\beta}(\mathrm{c},T) = \sum_{i=0}^{8}(a_{(\omega,\beta)i} + b_{(\omega,\beta)i}\cdot T)\cdot c^{i},\ 300\,\mathrm{K} \le T \le 1200\,\mathrm{K} \quad (2)$$

where a_i and b_i are polynomial coefficients [Table 1].

Phase field model of β → ω transformation in Ti-Nb

The orientation relationship (OR) between the β and ω phases derived from the selected area electron diffraction patterns (SADP) is[1], $\{111\}_{\beta}||\{0001\}_{\omega}$, $<\bar{1}10>_{\beta} \| <11\bar{2}0>_{\omega}$, and $<2\bar{1}\bar{1}>_{\beta} \| <0\bar{1}10>_{\omega}$, as shown in Figure 2. The OR is accomplished by a combination of a $\{2\bar{1}\bar{1}\}\langle 111\rangle_{\beta}$ huffle and a $\{211\}\langle 1\bar{1}\bar{1}\rangle_{\beta}$ shear and is the same in the athermal and isothermal ω[21]. There are four possible $<111>_{\beta}$ planes parallel to the $\{0001\}_{\omega}$, so there exist four crystallographic variants of the ω. The β ↔ ω transformation is thought to be a shuffle-dominated process[28] since it does not change the specific volume and has small temperature hysteresis; thus, the non-conserved structural order parameter is the shuffle degree η. A set of four structural order parameters η_p (p = 1, 2, 3, 4) is used to describe the four variants of the ω phase, η_p = 0 represents the parent phase β, $0 < \eta_p < 1$ represents the partially collapsed ω, and η_p = 1 represents the fully collapsed ω.

Therefore, the ω + β two-phase microstructure is characterized by two sets of order parameters, i.e., Nb concentration (mole fraction) c and shuffle degree η, and the total free energy of the system is formulated as:

$$F = \int d^{3}r[f_{ch} + f_{gr}] + E_{el} \quad (3)$$

Table 1. The coefficients, a_i and b_i, in the Gibbs energy polynomial

Parameters (J/mol)	a_0	a_1	a_2	a_3	a_4	a_5	a_6	a_7	a_8
ω	-3,078.0	13,137.0	-2,510.0	-5.16E-5	8.79E-4	-2.53E-3	3.31E-3	-2.06E-3	4.98E-4
β	1.19E-6	13,075.0	-13,075.0	-4.92E-3	1.57E-2	-2.83E-2	2.88E-2	-1.55E-3	3.40E-3
Parameters (J/mol)	b_0	b_1	b_2	b_3	b_4	b_5	b_6	b_7	b_8
ω	4.05837	-39.349	188.342	-827.930	2,501.50	-4,646.38	5,117.69	-3,059.05	764.763
β	-0.08363	-38.9304	188.342	-827.930	2,501.50	-4,646.37	5,117.69	-3,059.05	764.763

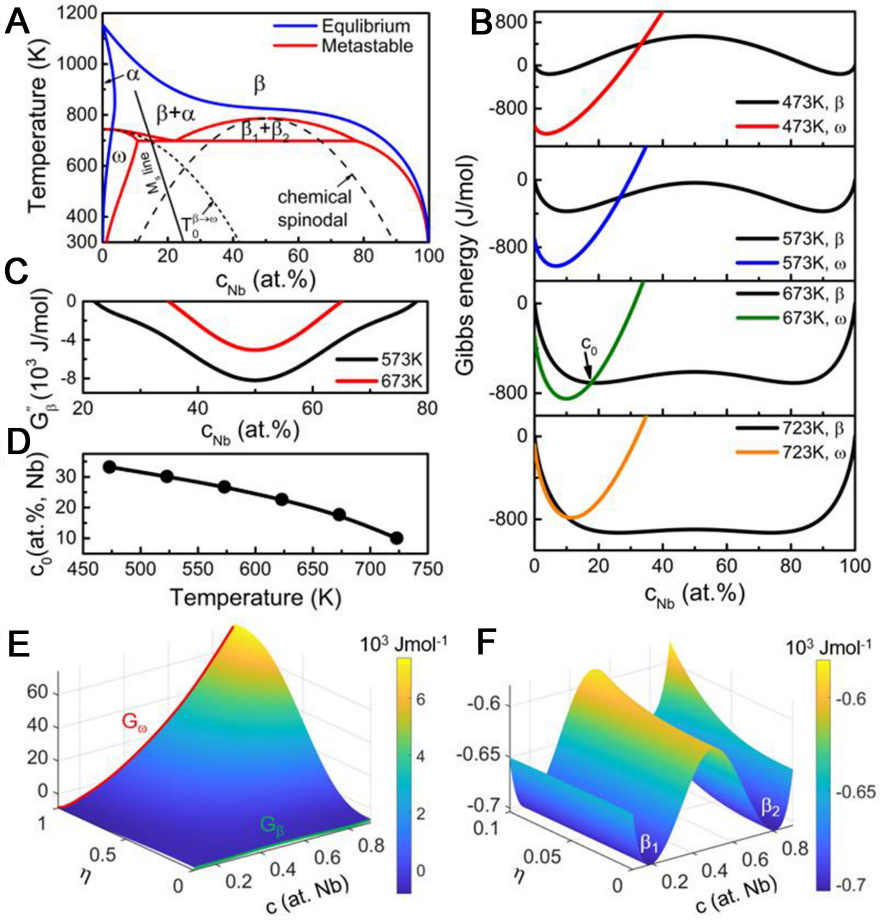

Figure 1. Thermodynamic results of Ti-Nb binary system. (A) Calculated equilibrium phase diagram (blue solid lines) and metastable phase diagram considering the β and ω phases (red solid line), where the spinodal decomposition occurs within the regions below the chemical spinodal. The T_0 curve for metastable β and ω equilibrium is also shown by the black shot dash line; the Ms line for β → α" is based on[4]; (B) Gibbs energy curves of the metastable β and ω phases at different temperatures; (C) The second derivatives of the Gibbs energy of the β phase at 573 K and 673 K, respectively, which define the spinodal regions (24.0 at.% < $\bar{c}$ < 76.0 at.%) at 573 K and (31.0 at.% < $\bar{c}$ < 69.0 at.%) at 673 K; (D) The critical concentration value, $c_0(T)$, obtained from the intersection point of the β and ω Gibbs energy curves at different temperatures (c_0 = 26.7 at.% and 17.7 at.% at 573 K and 673 K, respectively); (E) The chemical free energy surface $f_{ch}(c,\eta)$ of the Ti-Nb system in both the composition and structural order parameter space at 673 K, showing G and G at η = 0 and η = 1, respectively; (F) Enlarged chemical free energy surface at η =0, showing spinodal decomposition of the β matrix.

where f_{ch}, f_{gr}, and E_{el} represents the chemical free energy density, the gradient energy density, and the elastic energy, respectively, and d^3r means the integral of the chemical free energy density and gradient energy density of the computational cells. The chemical free energy surface $f_{ch}(c, \eta)$ in total free energy F has been adopted by using an interpolation function $h(\eta)$[29]:

$$f_{ch} = \sum_{p=1}^{4} h(\eta_p) G_\omega(c,T) + \left(1 - \sum_{p=1}^{4} h(\eta_p)\right) G_\beta(c,T) + \Phi_1 \sum_{p \neq q} \eta_p \eta_q + \Phi_2 \sum_{p=1}^{4} (\eta_p^2 - 2\eta_p^3 + \eta_p^4) \quad (4)$$

where $h(\eta_p) = \eta_p^3(6\eta_p^2 - 15\eta_p + 10)$ satisfies that $h(0) = 0$, $h(1) = 1$, and $dh/d\eta = 0$ at $\eta = 0$ and 1. As shown in Figure 1E and F, $\eta = 0$ corresponds to the Gibbs energy curve of the metastable β phase (Nb-lean β_1 + Nb-rich β_2), G_β, and $\eta = 1$ corresponds to the Gibbs energy curve of the ω phase, G_ω. The ϕ_1 represents the energy barrier between two different ω variants along the minimum energy path on the local chemical-free energy landscape, and ϕ_2 characterizes the energy barrier between the β and ω phases. The gradient energy density is[30]:

$$f_{gr} = \frac{1}{2}\kappa_c (\nabla c)^2 + \frac{1}{2}\kappa_\eta \sum_{p=1}^{4} (\nabla \eta_p)^2 \quad (5)$$

where k_c and k_η are the gradient coefficients of concentration and structure fields, respectively. The elastic energy is calculated via the microelasticity theory of Khachatuyan under the homogeneous modulus assumption (i.e., the β and ω phases are assumed to have the same elastic modulus)[31]:

$$E_{el} = \frac{1}{2} \sum_{p=1}^{4} \sum_{q=1}^{4} \int \frac{d^3k}{(2\pi)^3} B_{pq}(\boldsymbol{n}) \{\eta_p\}_k \{\eta_q\}_k^* \quad (6)$$

$$B_{pq}(\boldsymbol{n}) = C_{ijkl} \varepsilon_{ij}^{o}(p) \varepsilon_{kl}^{o}(q) - n_i \sigma_{ij}^{o}(p) \Omega_{jk}(\boldsymbol{n}) \sigma_{kl}^{o}(q) n_l \quad (7)$$

where C_{ijkl} is the elastic constants of the phase C_{11} = 128.5 GPa, C_{12} = 115.5 GPa, and C_{44} = 14.9 GPa[32]; $\Omega_{ij}^{-1}(\boldsymbol{n}) = C_{ijkl} n_k n_l$, and $\boldsymbol{n}$ is a unit vector in the reciprocal space. $\sigma_{ij}^{o}(p) = C_{ijkl}\varepsilon_{kl}^{o}(p)$ and $\varepsilon_{ij}^{o}(p)$ denotes the stress-free transformation strain (SFTS) of the pth variant for the β → ω transformation; then, the strain caused by β → ω transformation can be described in terms of the order parameter field, i.e., $\varepsilon_{ij} = \sum_{p=1}^{4} \varepsilon_{ij}^{o}(p) \eta_p^2$. The four SFTS tensors are calculated using the lattice constants a_β = 3.273 Å for the β phase and a_ω = 4.659 Å, c_ω = 2.819 Å for the ω phase in Ti-22 at.% Nb[32], and the Burgers correspondence between the β and ω phases [Figure 2], as shown in Table 2. In the reference coordinate N1, i.e., $x \| [2\bar{1}\bar{1}0]_\omega$, $y \| [\bar{1}2\bar{1}0]_\omega$, and $z \| [0001]_\omega$ in the basis of the ω phase, the transformation matrix that describes a homogeneous lattice deformation from β to ω is:

$$\varepsilon_{N1}^{\omega}=\begin{pmatrix}\frac{a_{\omega}-\sqrt{2}a_{\beta}}{\sqrt{2}a_{\beta}} & 0 & 0\\ 0 & \frac{a_{\omega}-\sqrt{2}a_{\beta}}{\sqrt{2}a_{\beta}} & 0\\ 0 & 0 & \frac{2c_{\omega}-\sqrt{3}a_{\beta}}{\sqrt{3}a_{\beta}}\end{pmatrix} \tag{8}$$

In the reference coordinate N2, i.e., $x||[100]_{\beta}$, $y||[010]_{\beta}$, and $z||[001]_{\beta}$ in the β phase, the SFTS of the four variants can be calculated by $\varepsilon^{\omega}(i)=T(i)\varepsilon_{N1}^{\omega}T(i)^{-1}$, where i = 1, 2, 3, and 4, and $T(i)$ is the rotation matrix mapping between N1 and N2 coordinates for the four variants:

$$\begin{aligned}T(1)&=\begin{bmatrix}-\frac{1}{\sqrt{2}} & -\frac{1}{\sqrt{6}} & \frac{1}{\sqrt{3}}\\ \frac{1}{\sqrt{2}} & -\frac{1}{\sqrt{6}} & \frac{1}{\sqrt{3}}\\ 0 & \frac{2}{\sqrt{6}} & \frac{1}{\sqrt{3}}\end{bmatrix}, T(2)=\begin{bmatrix}0 & \frac{2}{\sqrt{6}} & -\frac{1}{\sqrt{3}}\\ -\frac{1}{\sqrt{2}} & \frac{1}{\sqrt{6}} & \frac{1}{\sqrt{3}}\\ \frac{1}{\sqrt{2}} & \frac{1}{\sqrt{6}} & -\frac{1}{\sqrt{3}}\end{bmatrix},\\ T(3)&=\begin{bmatrix}-\frac{1}{\sqrt{2}} & \frac{1}{\sqrt{6}} & \frac{1}{\sqrt{3}}\\ 0 & \frac{2}{\sqrt{6}} & -\frac{1}{\sqrt{3}}\\ \frac{1}{\sqrt{2}} & \frac{1}{\sqrt{6}} & \frac{1}{\sqrt{3}}\end{bmatrix}, T(4)=\begin{bmatrix}\frac{1}{\sqrt{2}} & \frac{1}{\sqrt{6}} & \frac{1}{\sqrt{3}}\\ -\frac{1}{\sqrt{2}} & \frac{1}{\sqrt{6}} & \frac{1}{\sqrt{3}}\\ 0 & \frac{2}{\sqrt{6}} & -\frac{1}{\sqrt{3}}\end{bmatrix}.\end{aligned} \tag{9}$$

Considering the 2D simulation is on the $\{011\}_{\beta}$ plane (i.e., a typical zone axis SADP to observe ω structure)[33-35], the final results of SFTSs corresponding to the $(011)_{\beta}$ plane are:

$$\begin{aligned}
\varepsilon^{\omega}(1) &= \begin{bmatrix} 0.0011474 & -0.0003462 & -0.0002448 \\ -0.0003462 & 0.0007477 & 0.0001413 \\ -0.0002448 & 0.0001413 & 0.0006477 \end{bmatrix}, \\
\varepsilon^{\omega}(2) &= \begin{bmatrix} 0.0005478 & 0.0 & 0.0 \\ 0.0 & 0.0005478 & 0.0 \\ 0.0 & 0.0 & 0.0014472 \end{bmatrix}, \\
\varepsilon^{\omega}(3) &= \begin{bmatrix} 0.0005478 & 0.0 & 0.0 \\ 0.0 & 0.001347 & -0.0002827 \\ 0.0 & -0.0002827 & 0.0006477 \end{bmatrix}, \\
\varepsilon^{\omega}(4) &= \begin{bmatrix} 0.0011474 & 0.0003462 & 0.0002448 \\ 0.0003462 & 0.0007477 & 0.0001413 \\ 0.0002448 & 0.0001413 & 0.0006477 \end{bmatrix}.
\end{aligned} \tag{10}$$

Note that the SFTS for the β → ω transformation used in our simulation is assumed to be independent of concentration.

The stochastic Cahn-Hillardand time-dependent Ginzburg-Landau equations[30,36] are used to govern the equations of the concentration and structural order parameters, respectively.

$$\frac{\partial c}{\partial t} = \nabla\left[M\nabla\frac{\delta F}{\delta c} \right] + \zeta_c \tag{11}$$

$$\frac{\partial \eta_p}{\partial t} = -L\frac{\delta F}{\delta \eta_p} + \zeta_\eta, p = 1-4 \tag{12}$$

where $M = \frac{1}{RT}\exp(\frac{\phi}{RT})$ is the chemical mobility and derived from the interdiffusion coefficients, $\phi = (1\text{-}c)\phi^{\mathrm{Ti}} + c\phi^{\mathrm{Nb}} + c(1\text{-}c)\phi^{\mathrm{Ti,Nb}}$ is activation enthalpy, ϕ^{Ti} and ϕ^{Nb} are the mobility parameters for pure Ti and Nb, respectively, $\phi^{\mathrm{Ti,Nb}}$ is binary interaction parameter in the Ti-Nb binary system[37], and L = 8.82 × 10^{-11} $m^3 \cdot J^{-1} \cdot s^{-1}$[38] is the structural mobility of the structural order parameter. ζ_c and ζ_η are the Langevin stochastic noise terms characterizing thermal fluctuations and are used to describe the nucleation process through a Gaussian-distributed random number generator ρ_i[39]:

$$\zeta_c(\mathbf{r},t) = \sqrt{2\mathbf{k}_{\mathbf{B}}TM/(l_0{}^d\Delta t)}\nabla\cdot\rho \tag{13}$$

$$\zeta_\eta(\mathbf{r},t) = \sqrt{2k_BTL/(l_0{}^d\Delta t)}\rho \tag{14}$$

Table 2. Lattice correspondence between β and ω phases

Variant	$<2\bar{1}\bar{1}0>_\omega$	$<\bar{1}2\bar{1}0>_\omega$	$<0001>_\omega$	$\{0001\}_\omega$
1	$[\bar{1}10]_\beta$	$[\bar{1}\bar{1}2]_\beta$	$[111]_\beta$	$(111)_\beta$
2	$[0\bar{1}1]_\beta$	$[112]_\beta$	$[\bar{1}11]_\beta$	$(11\bar{1})_\beta$
3	$[\bar{1}01]_\beta$	$[121]_\beta$	$[1\bar{1}1]_\beta$	$(1\bar{1}1)_\beta$
4	$[1\bar{1}0]_\beta$	$[211]_\beta$	$[11\bar{1}]_\beta$	$(\bar{1}11)_\beta$

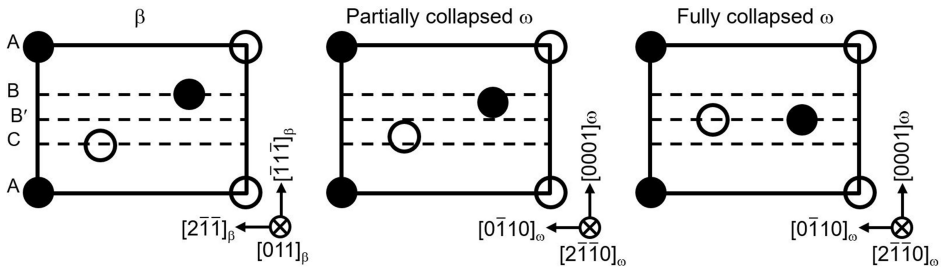

Figure 2. Schematic representations of the crystallographic relationship between the β and ω phases in their relevant crystallographic directions.

where l_0 is the grid size, d is the dimensionality of the space, Δt is the time step, and ρ is a d-dimensional vector.

For nondimensionalization, the energy normalization factor E_{normal} is 40 KJ·mol^{-1}, the dimensionless energy barriers are $\Phi_1^* = 0.06$ and $\Phi_2^* = 0.01$[40], and the dimensionless gradient energy coefficients are chosen to be $k_c^* = 6.0$ and $k_\eta^* = 0.025$[41], guaranteeing a diffused interface profile and yielding dimensionless interfacial energy between the β and ω phases, $\gamma^* = 0.095$; thus, the numerical grid size is determined to be $l_o \sim 1$ nm based on the relation $l_0 = \frac{\gamma}{\gamma^* \cdot (E_{normal}/V_m)}$ [41], where the interfacial energy γ of (111)/(0001) is ~380 mJ·m^{-2}[20], and the molar volume $V_m = 1 \times 10^{-5}$ m^3·mol^{-1} is assumed for the system. The dimensionless structural mobility parameter is $L^* = 1.0$ to ensure a diffusion-controlled process[41]. Except for $\zeta_c = 0$ upon aging at 573 K in Ti-26 at.% Nb, the amplitude of dimensionless noise ζ_c^* is [-0.00025, 0.00025] to produce a minor concentration variation relative to the initial Nb content of the β matrix. The amplitude of dimensionless noise ζ_η^* is [-0.0022, 0.0022], which is determined via the numbers of the athermal nuclei at transformation temperature (ω_s) in Ti-26 at.% Nb upon water quenching, i.e., the athermal ω nuclei uniformly distribute in the computational cells, and the ζ_η^* is the same value upon aging. The system size used in the simulations is $512l_o \times 512l_o$. Periodic boundary conditions are applied along all three dimensions. All the dimensionless parameters used in the simulations are listed in Table 3.

RESULTS AND DISCUSSION

Gibbs energy curves of ω and β phases

Figure 1B shows the Gibbs energy curves of the ω and β phases as functions of Nb concentration and temperature. A metastable β miscibility gap can be found in the Ti-Nb binary system with a critical temperature of ~786 K [Figure 1A], and the spinodal regions are 24.0 at.% < $\overline{c}$ < 76.0 at.% at 573 K and 31.0 at.% < $\overline{c}$ < 69.0 at.% at 673 K [Figure 1C]. The critical concentration $c_0(T)$ at the intersection point of the ω and β Gibbs energy curves shows a parabolic increase with decreasing temperature, as shown in Figure 1D. When the alloy composition is less than $c_0(T)$, congruent β → ω transformation will take place, followed by the rejection of Nb from the phase. When the alloy composition is slightly larger than $c_0(T)$ with a $\Delta c = c - c_0 \leq 2$ at.%[40], peudospinodal decomposition could occur, which is defined as a phase transformation mechanism with continuous composition changes of non-isostructural phases. When the

Table 3. Dimensionless parameters used in the simulation

Energy barrier[40]	$\Phi_1^* = 0.06$, $\Phi_2^* = 0.01$
Gradient energy coefficients[41]	$k_c^* = 6.0$, $k_\eta^* = 0.025$
Interface mobility[41]	$L^* = 1.0$
Langevin stochastic noise	ζ_c^* = [-0.00025, 0.00025], ζ_η^* = [-0.0022, 0.0022] ($\zeta_c^* = 0$ upon aging at 573 K in Ti-26 at.%Nb)

alloy composition is larger than $c_0(T)$ with a $\Delta c > 2$ at.% and outside the spinodal regions at the two temperatures considered, only the conventional nucleation-and-growth mechanism can be activated for the $\beta \rightarrow \omega$ transformation.

Microstructural evolution in Ti-26 at.% Nb

Formation of athermal ω

2D simulations of athermal ω transformation in Ti-26 at.% Nb are first carried out upon water quenching, and the results are shown in Figure 3. The water quenching process is from 1,173 K to 300 K. To show the detailed evolution of the ω, we zoom into the initial microstructures according to Figure 3A and show the enlarged images in Figure 3B. Figure 3B1-B4 shows the 2D simulation results of concentration fields, while Figure 3B5-B8 shows the corresponding structural order parameter fields. Athermal ω nanodomains with ellipsoidal shapes are formed via diffusionless structural transformation upon cooling since the concentration fields keep the initial Nb content. The number and average size of ω precipitates increase with decreasing temperature, and the final average size of ω nanodomains is less than 5 nm at 300 K. Thermodynamically, a spinodal region of T < 604 K exists at Ti-26 at.% Nb [Figure 1A], but the absence of the spinodal decomposition indicates the lack of driving force to defeat the gradient energy or dynamic difficulty for interdiffusion upon water quenching in Ti-26 at.% Nb. Moreover, athermal ω nanodomains have been found in Ti-19 at.% V without solute partitioning or composition fluctuations after water quenching from 1,173 K to room temperature via transmission electron microscope (TEM) and APT observations[42], although a larger spinodal region of T < 969 K theoretically exists in the Ti-19 at.% V[27]. Based on the above analysis, we believe that the smaller driving force is the major cause for the absence of phase separation in the alloy system with a lower Nb content.

The volume fraction of the athermal nanodomains is shown in Figure 3C and presents that the athermal ω phase in Ti-26 at.% Nb increases gradually upon cooling. In the diffusionless β → athermal ω transformation, the actual transformation temperature ω_s will be below the T_0 [Figure 1A] because supercooling is needed to provide the additional driving force for overcoming interfacial and elastic energies caused by the structural transformation of a new phase. In our current model, this condition has been considered by introducing gradient and elastic energies. The simulated start transition temperature ω_s of Ti-26 at.% Nb is ~375 K, which has a good agreement with previous experimental studies estimated by the electrical resistivity curve[17]. Figure 3D shows the related statistical distribution of the ω size and indicates that the size distribution is relatively uniform for the homogeneous ω nanodomains. The evolution of the average shuffle degree of ω upon cooling is shown in Figure 3E and displays that the athermal ω has a partially collapsed structure, and the shuffle degree increases with decreasing temperature and could help us to explain that the intensities of ω diffraction spots become higher at a lower temperature for Ti-Nb based alloys from $[011]_\beta$ SADP[8].

Formation of isothermal ω

According to the Gibbs energy curves in Figure 1B, c_0 (= 26.7 at.%) is higher than the alloy concentration; thus, the Gibbs energy of the ω phase is lower than the β phase at 573 K. As a result, a spontaneous

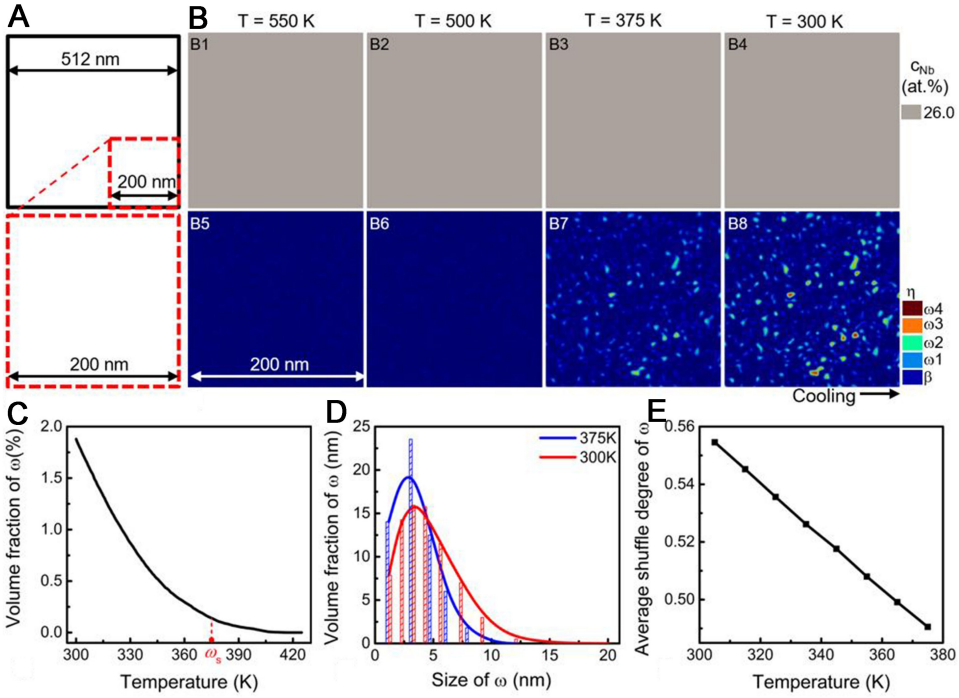

Figure 3. 2D simulations of athermal ω transformation in Ti-26 at.% Nb upon water quenching. (A) Schematics of zooming into the microstructure; (B) Enlarged images showing microstructures of athermal ω nanodomains in the β matrix, as indicated in (A), where (B1-B4) show the concentration fields, and (B5-B8) show the structural order parameter fields. The four ω variants are presented in different colors, and the β matrix is represented in blue; (C) Change in volume fraction of athermal ω upon cooling; (D) Size distribution of athermal ω nanodomains; (E) Variation of the average shuffle degree of athermal ω nanodomains.

nucleation process of isothermal ω can be found at 573 K via congruent transformation followed by Nb depletion from ω particles to β matrix, and four ω variants nucleate randomly with an equal probability at the beginning. Figure 4 shows the microstructural evolution of particles during isothermal aging at 573 K in Ti-26 at.% Nb alloy, where Figure 4A shows the concentration evolution during aging at 573 K, Figure 4B shows the corresponding one-dimensional (1D) concentration waves along the white short dash lines of the computational cell, and Figure 4C shows the morphological evolution during aging at 573 K. Ellipsoidal ω precipitates with a finer size have formed after a short time aging of 0.2 h, but the corresponding Nb content of the isothermal ω is same as the β matrix. Such rapid congruent transformation from the β matrix has also been found in α precipitation for alloy systems with lower solute content during aging[40,43]. With increasing aging time, the number and size of isothermal particles increase; meanwhile, the Nb content of ω gradually decreases. The size distribution of ω particles is found to be time-dependent, as shown in Figure 4D, and gradually becomes wider with increasing aging time. The larger ω particles with a small volume fraction can grow up to > 40 nm, while the smaller ω nuclei with a size < 10 nm can also coexist at a longer aging time. Moreover, both the number and average size of isothermal ω formed at 573 K for 1 h are larger than that of athermal ω nanodomains [Figure 3], which is consistent with a previous experimental study in Ti-26 at.% Nb[5].

But at 673 K, the formation of isothermal ω in Ti-26 at.% Nb is activated by conventional nucleation-and-growth mechanism, which microstructural evolution is shown in Figure 5. The alloy composition of Ti-26 at.% Nb is much larger than c_0 (= 17.6 at.%) and outside the spinodal region at 673 K [Figure 1]; thus, the congruent transformation and other mechanisms assisted by spinodal decomposition cannot be accomplished. Redistribution of Nb via long-range diffusion is needed for the nucleation of isothermal

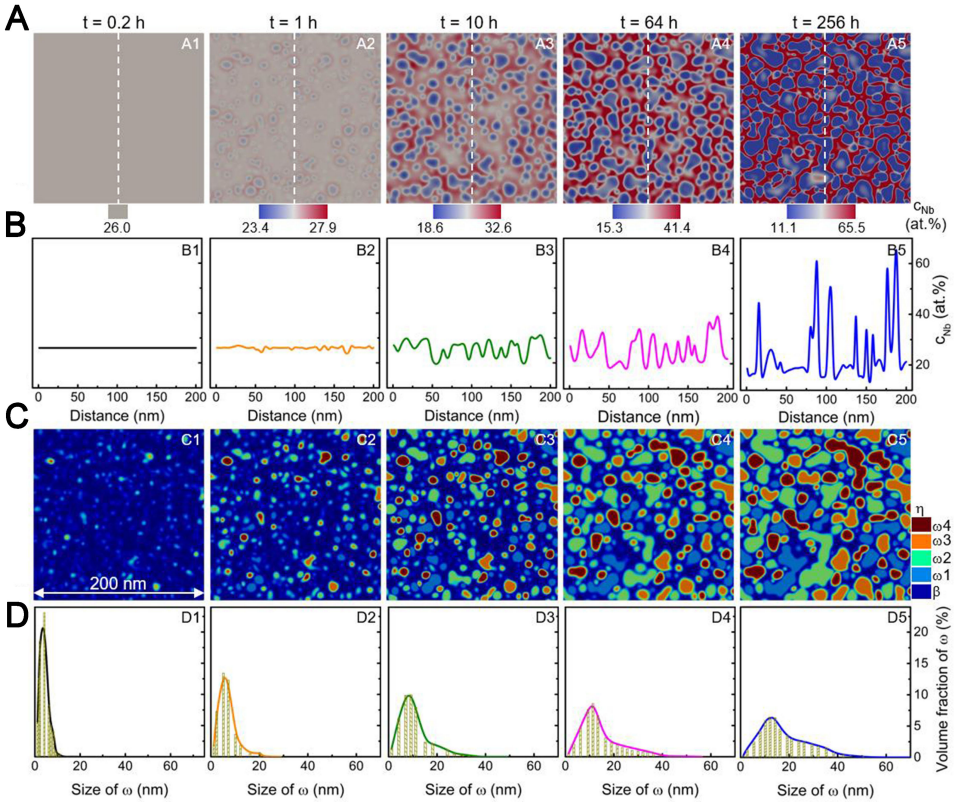

Figure 4. Calculated microstructural evolution of isothermal ω aged at 573 K for different aging times in Ti-26 at.% Nb. (A) Concentration fields; (B) One-dimensional Nb concentration profiles along the white short dash line of the computational cells shown in (A); (C) Structural order parameter fields; (D) Size distribution of isothermal particles.

particles, and the Nb content of initial ω nuclei has been found near the equilibrium composition of ω (c_ω = 10.2 at.%), which is a typical characteristic for a conventional nucleation and growth process[40]. The nucleation density of the isothermal ω particles formed at 673 K is visibly low than that formed at 573 K [Figure 4], and the particle density also decreases with increasing aging time with a corresponding larger size at 673 K. The phenomena are universal for decreased density and coarsening at higher aging temperatures and longer aging time and have also been found in other precipitation such as Ni_4Ti_3[44] and α[45]. Moreover, previous literature has observed high-density finer ω precipitates after aging at 673 K for 1 h in Ti-26 at.% Nb[5]. But in our current simulations, the isothermal ω is not found during aging at 673 K within 2.5 h, and we deduce that the reported ω particles may be athermal ω nanodomains formed upon cooling from 673 K to room temperature after aging at 673 K for 1 h. The simulations and reasoning can help us to understand that[5] the average size of particles formed after aging at 673 K for 1 h is smaller than that formed after aging at 573 K for 1 h.

Microstructural evolution in Ti-50 at.% Nb

Formation of athermal ω

For alloy composition within the spinodal region, thermal processing, including solution treatment and isothermal aging, can create a special transformation pathway, i.e., concentration modulations produced by the spinodal decomposition of the β phase followed by ω formation. Phase field simulations of athermal formation in Ti-50 at.% Nb upon water quenching from 1,173 K to 300 K are shown in Figure 6. A wide temperature range (300 K < T < 786 K) for spinodal regions exists in Ti-50 at.% Nb [Figure 1A], leading to precursory concentration modulations with a wavelength of ~ 10 nm before the formation of athermal ω,

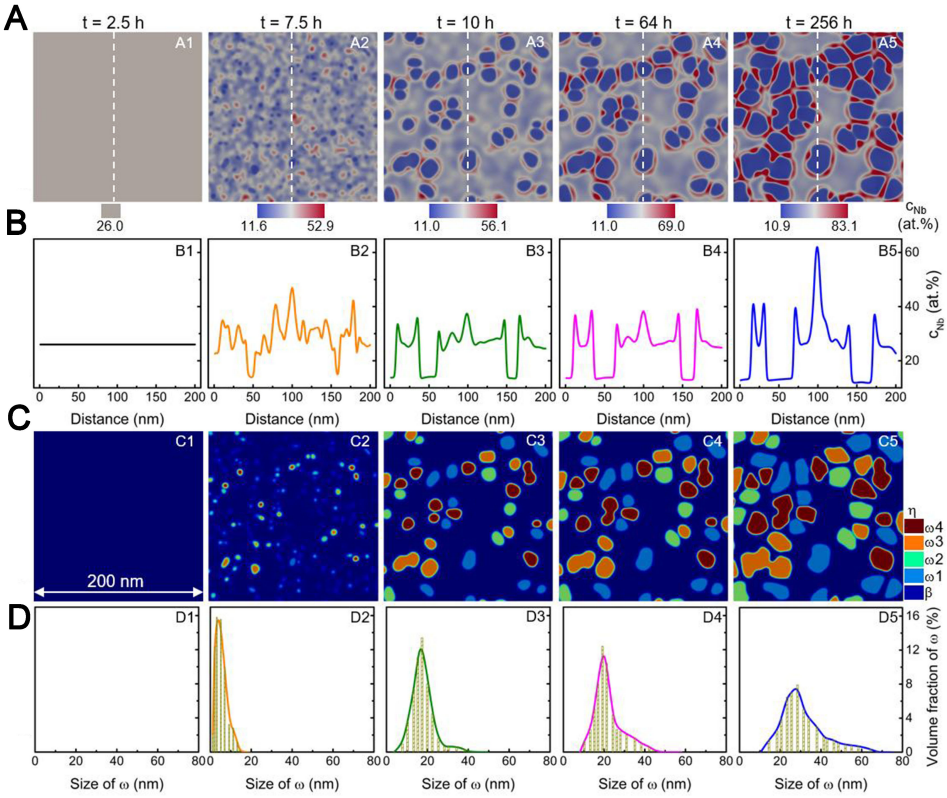

Figure 5. Calculated microstructural evolution of isothermal ω aged at 673 K for different aging times in Ti-26 at.% Nb. (A) Concentration fields; (B) One-dimensional Nb concentration profiles along the white short dash line of the computational cells shown in (A); (C) Structural order parameter fields; (D) Size distribution of isothermal ω particles.

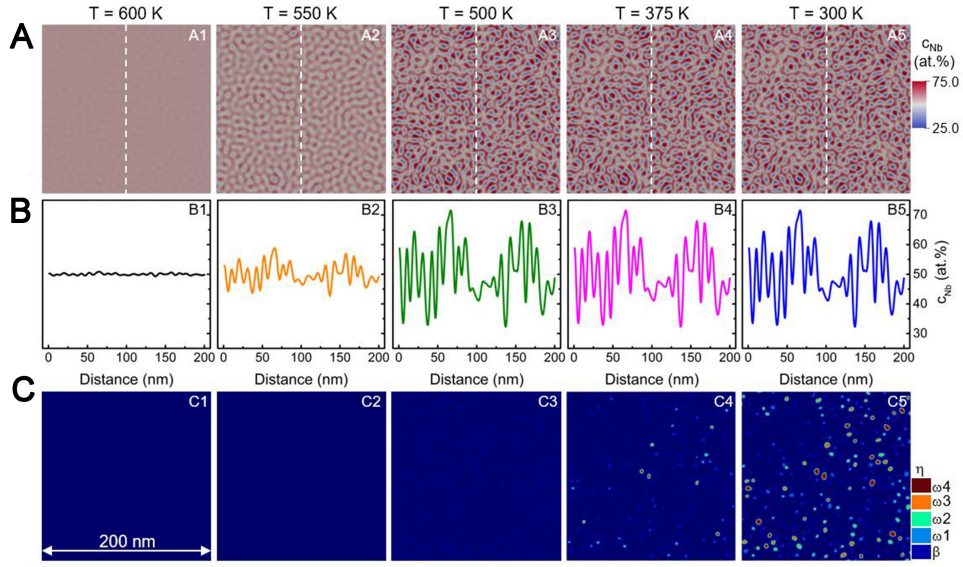

Figure 6. Calculated microstructural evolution of athermal ω formed upon water quenching in Ti-50 at.% Nb. (A) Concentration fields; (B) One-dimensional Nb concentration profiles along the white short dash line of the computational cells shown in (A); (C) Structural order parameter fields.

which is different from that in Ti-26 at.% Nb upon water quenching [Figure 3]. The Nb-rich β_2 regions (red color) form a continuous matrix while the Nb-lean β_1 regions (blue color) form uniformly distributed islands, and the amplitude of spinodal decomposition increases upon cooling at T ≥ 500 K. But at T < 500 K, no significant changes can be found in the spatial distribution and amplitude of spinodal decomposition by virtue of the low mobility at low temperatures[37]. Figure 6C exhibit that finer dispersed ω nanodomains form at the solute-lean β_1 islands, which number density and size are smaller than that formed in Ti-26 at.% Nb upon water quenching [Figure 3]. The unchanged concentration fields at T < 500 K indicates that the $\beta \rightarrow \omega$ phase transformation in Ti-50 at.% Nb upon water quenching also is diffusionless transformation, and the formed ω structure is athermal ω nanodomains assisted by the precursory spinodal decomposition. The ω formed in Nb-lean β_1 regions has also been found in compositionally modulated Ti-23Nb-2O (at.%) alloy via APT and TEM observations after solution treatment[14].

Formation of isothermal ω

c_0 (= 26.7 at.%) is much higher than the equilibrium concentration of a β_1 phase (~ 10.0 at.% at 573 K) at 573 K [Figure 1]; thus, the phase has a lower Gibbs energy in the β_1 regions for Ti-50 at.% Nb. Figure 7 shows the microstructural evolution of ω precipitates during isothermal aging at 573 K in Ti-50 at.% Nb alloy. The spinodal decomposition preferentially occurs with a wavelength of ~ 8 nm smaller than that obtained upon water quenching, which amplitude gradually increases with aging time. Spinodal decomposition is a general state and has been experimentally found in many aged Ti-Nb-based alloys[3,24,46,47] and other aged alloy systems such as CuNi-based alloys[48], Fe-Cr alloys[49], U-Zr alloy[50], and high-entropy alloys[51,52] via X-ray differaction (XRD), TEM, scanning transmission electron microscopy (STEM), APT, and small-angle neutron scattering (SANS) analysis, showing temperature dependence and time dependence.

When the concentration of β_1 regions is lower than c_0, these regions transform into a mixture of ω + β phases with fine-scale via displacive transformation. The concentration of the β_2 regions is much higher than c_0 and gradually evolves towards the equilibrium composition of the β phase (c_β = 91.3 at.% at 573 K); thus, the β_2 regions become -free zones. ω embryos have been detected in solute-lean regions caused by spinodal decomposition in aged alloy[25,26]. Moreover, the β_1/β_2 interfaces present high structural stability during aging at 573 K [Figure 7A], during which spatial distribution remains virtually unchanged upon the aging process and has a significant geometric constraint on the growth of ω domains; thus, a confined size of ω particles is found in the smaller β_2 islands even after long-time aging. Therefore, the morphology patterns of spinodal decomposition regulate the spatial distribution of ω precipitates in Ti-50 at.% Nb.

At 673 K, the equilibrium concentration of the Nb-lean β_1 regions (~18.3 at.%) is slightly larger but very close to c_0 (= 17.6 at.%). These regions will transform into a mixture of ω + β phases via the pseudospinodal mechanism[Figure 8]. The Nb-lean β_1 regions are uniformly distributed channels formed at 673 K. The amplitude of the spinodal decomposition gradually increases until the equilibrium concentrations are reached, then the wavelength increases from the initial ~13 nm to ~20 nm with further aging. Previous experimental studies have reported that the wavelength increases with increasing aging temperature[24], and our simulations supply that the aging temperature can also regulate the spatial distribution of β_1 regions, which can help us to explain that[2,23,24] the morphology of α" changes from spherical nanodomains to a plate-like structure with increasing temperature.

The transformation sequence, i.e., wavelength increases followed by the isothermal ω formation, is attributed to the fact that no barrier exists in the spinodal decomposition, but thermal fluctuations of concentration and structure are needed for the ω formation via the pseudospinodal mechanism. A thermal fluctuation of concentration is required to bring local concentration in β_1 to the left of c_0, and a thermal

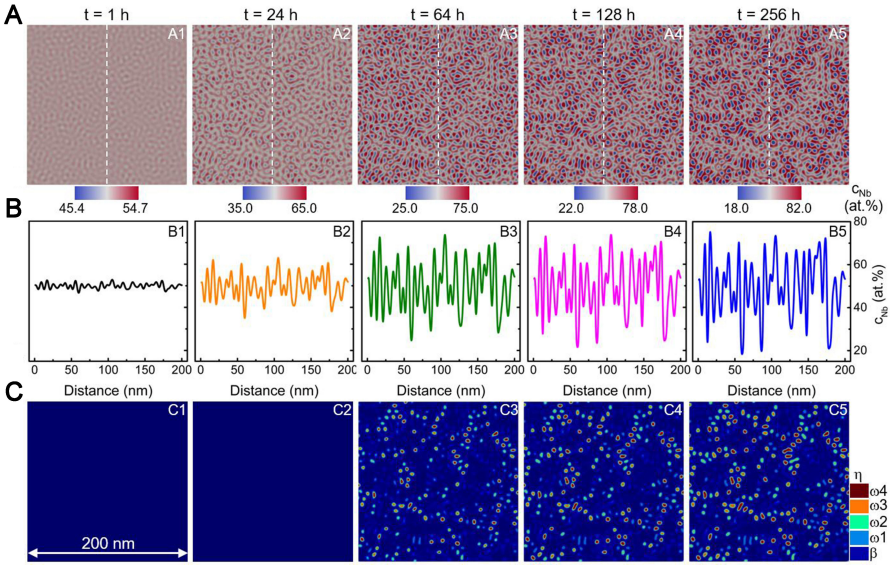

Figure 7. Calculated microstructural evolution of isothermal ω aged at 573 K for different aging times in Ti-50 at.% Nb. (A) Concentration fields; (B) One-dimensional Nb concentration profiles along the white short dash line of the computational cells shown in (A); (C) Structural order parameter fields.

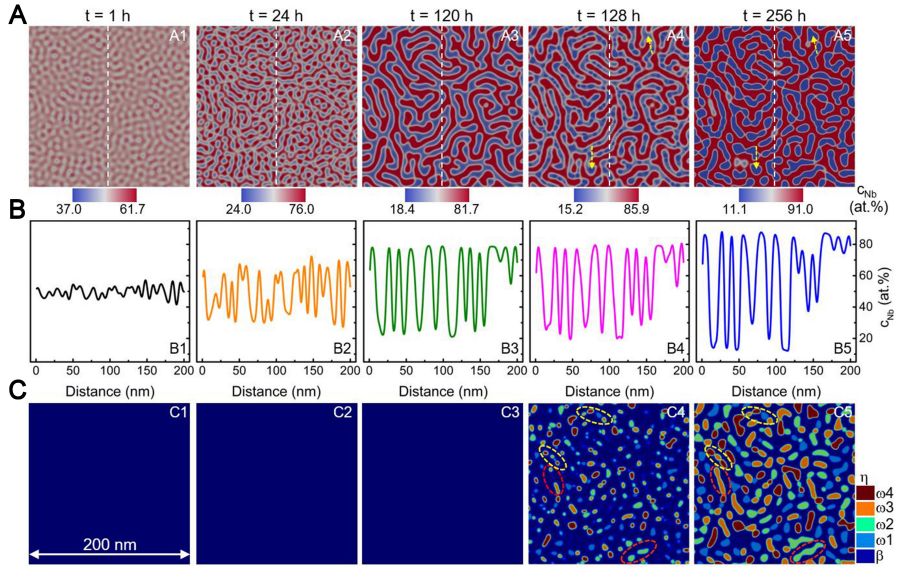

Figure 8. Calculated microstructural evolution of isothermal ω aged at 673 K for different aging times in Ti-50 at.% Nb. (A) Concentration fields; (B) One-dimensional Nb concentration profiles along the white short dash line of the computational cells shown in (A); (C) Structural order parameter fields.

fluctuation of structure is also required for structural transformation from bcc to hexagonal. Then, isothermal ω precipitates can be nuclear and grow, which concentration gradually decreases towards the equilibrium composition of the ω phase (c_{ω} = 10.2 at.% at 673 K) with increasing aging time. The distribution of isothermal ω particles is also confined in the β_1 channels at 673 K. This phase transformation pathway via pseudospinodal has also been found in precipitation with precursory spinodal decomposition[40].

Furthermore, it is noteworthy that the size and shape of particles are decided by two main reasons. First is the morphological patterns of the concentration modulations produced by the spinodal decomposition. The interconnected β_1 channels obtained at 673 K provide more space for the growth of ω than the dispersed β_1 islands formed at 573 K. Thus, an elongated shape of ω precipitates can be found overall during 673 K aging. The β_1 channels formed at 673 K have a certain degree of orientation. The ω precipitates with their habit planes parallel to the channels have extensive growth and elongated shape, while those with their habit planes perpendicular to the channels (marked by yellow arrows in Figure 8A) experience limited growth and show spherical-like shape due to the geometric constraint of the solute-rich β_2 matrix. Moreover, experimental observations have found that[19] the oxygen could regulate the morphology of isothermal ω in Ti-20Nb-*x*O (at.%) alloys aged at 723 K for 144 h, i.e., initial ellipsoid shape changes to elongated rod shape as oxygen content increasing from 0.1 at.% to 3.4 at.%. Theoretical study[53] has shown that the spatial distribution of solute-lean β_1 can change from spherical islands to interconnected channels in Ti-23Nb-*x*O (at.%) aged at 1,073 K with increasing oxygen content from 1 at.% to 5 at.%. From our simulations and the above analysis, we summarize that the morphological patterns of spinodal decomposition can regulate the size and shape of the ω precipitates. Second is the nucleation sites of ω variants. Each ω variant has the same probability of nucleating by thermal fluctuations. When several ω variants (generally ≥ 3) nucleate in adjacent positions of β_1 channels (marked by yellow circles in Figure 8C), these ω particles tend to experience limited growth, whereas the dispersed variants have a faster growth rate and larger size (marked by red circles in Figure 8C).

Mechanisms of ω formation during isothermal aging

The above simulations indicate that the formation mechanism for isothermal ω depends sensitively on alloy composition and aging temperature. To examine more details of the microstructure during aging at two different aging temperatures, volume fraction, number, average area, and average shuffle degree of the isothermal ω particles at two alloy compositions are plotted as a function of aging time, and the results are exhibited in Figure 9. The statistical system size is 512 nm 512 nm. Figure 9A shows the volume fraction of the isothermal ω precipitates for four aging conditions. This volume fraction curve in Ti-26 at.% Nb aged at 573 K enables us to split the ω dynamics into two characteristic stages of nucleation regime (≤ 10 h) and growth regime (> 10 h), whereas the other curves can be divided into three stages, including incubation period without ω phase (stage I), nucleation regime (stage II), and growth regime (stage III). The incubation time increases with increasing alloy composition (~40 h for Ti-50 at.% Nb at 573 K) and aging temperature (i.e., ~5 h for Ti-26 at.% Nb at 673 K and ~120 h for Ti-50 at.% Nb at 673 K). During the incubation period, Ti-26 at.% Nb aged at 673 K experiences composition redistribution [Figure 5], while Ti-50 at.% Nb produces spinodal decomposition at two aging temperatures [Figures 7 and 8]. During the nucleation stage, multiple nuclei can form within a smaller time window that increases with increasing alloy composition.

Ti-26 at.% Nb alloy has a larger volume fraction of isothermal ω particles at two aging temperatures, and the volume fraction decreases with increasing aging temperature, which indicates the congruent transformation process promotes the formation of ω particles with a larger volume fraction as compared with the conventional nucleation-and-growth reaction. The evolution rates of ω volume fractions are similar in Ti-26 at.% Nb at two aging temperatures but have a significant difference in Ti-50 at.% Nb. For Ti-50 at.% Nb, the ω volume fraction gently evolves at 573 K and has limited growth at stage III (> 70 h), but it develops more sharply at 673 K. This difference is attributed to the fact that the β_1 regions formed at 673 K have lower Nb content with larger centralized spaces [Figure 8] than that formed at 573 K [Figure 7].

The number and average area of isothermal precipitates are shown in Figure 9B and C. From alloy composition, the number of isothermal ω particles formed in Ti-50 at.% Nb is overall larger than that formed in Ti-26 at.% Nb, but the average ω area in Ti-50 at.% Nb is noticeably smaller than that in Ti-26

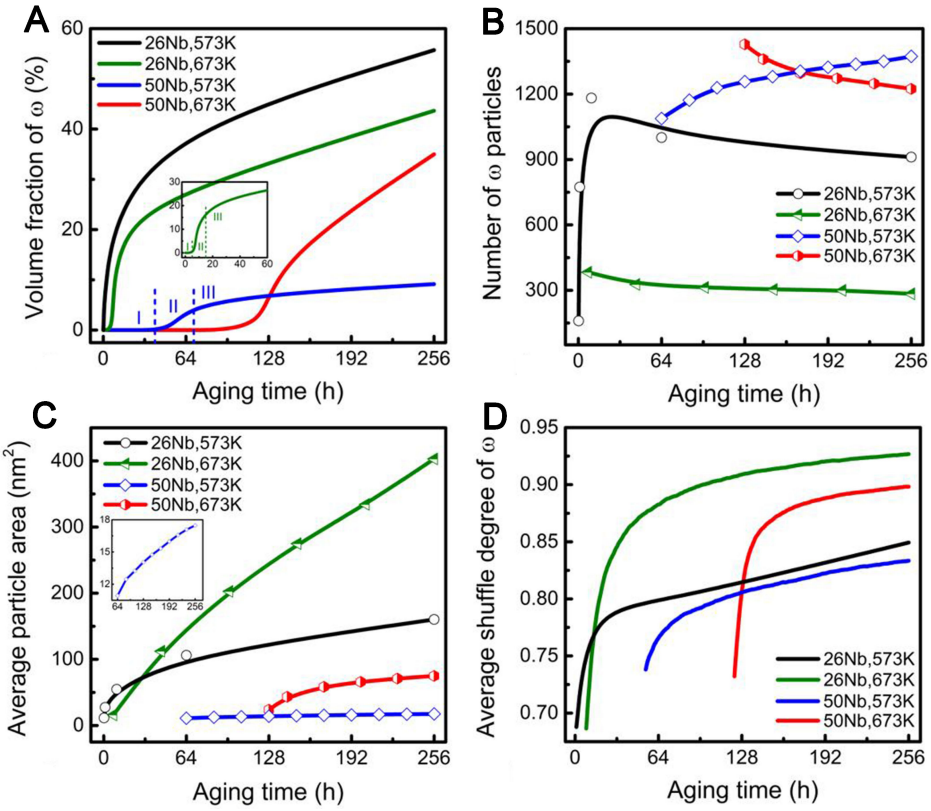

Figure 9. Statistical analysis of isothermal ω precipitates at different aging temperatures for different average compositions. (A) Volume fraction change of ω; (B) The number of ω particles; (C) The average area of ω particles, where the inset describes the area evolution of Ti-50 at.% Nb during aging at 573 K; (D) Variation of the average shuffle degree of the isothermal ω precipitates.

at.% Nb. From aging temperature, the number of ω particles formed at 673 K gradually decreases with increasing aging times in two alloy compositions, and the corresponding average areas gradually increase as the aging process. But at 573 K, Ti-26 at.% Nb has a linear increase in the number of ω particles at the nucleation regime, then gradually decreases during the growth stage and shows a continuous increase of the average particle area. Whereas, Ti-50 at.% Nb exhibits a monotonic but non-linear increase in the number of ω particles and a sluggish increase of particle size during the nucleation and growth regimes.

The evolution of the average shuffle degree of the isothermal ω is shown in Figure 9D. Overall, the average shuffle degree of the isothermal does not reach completion (= 1) within 256 h aging but is noticeably larger than that of the athermal ω [Figure 3E]. Moreover, the shuffle degree of ω particles increases sharply at a certain time window (> nucleation stage) and then evolves gently at a longer aging time. It can be understood from the evolution results of concentration fields. According to the Gibbs energy curves [Figure 1B], a lower Nb content decreases the Gibbs energy of the whole system. Experimental observations have also shown that the collapse degree of $\{222\}_\beta$ planes in athermal ω increases with decreasing solute content[17,42]. At the initial formation stage of the isothermal ω, including the nucleation regime, a conspicuous depletion of Nb from ω particles can be found, which can cause a relatively sharp increase of shuffle degree in ω particles, but the Nb content of the ω particles will be close to the equilibrium composition of ω phase at a longer aging time, the evolution of concentration fields will become gentle thus slow the increase rate of shuffle degree. This description can also explain that a higher aging temperature accelerates the increase of shuffle degree and brings about a larger shuffle value [Figure 9D] since a higher temperature has a larger diffusion coefficient and accelerates the Nb depletion from ω precipitates[37].

Comparison with O' and α" nanodomains

O' and α" nanodomains have also been found in Ti-Nb-based ferroelastic systems upon cooling and change the sharp, discontinuous martensitic transformation into a continuous transition over a wide temperature range[2,4]. Theoretical calculations have shown no energy barrier in the transformation of β → O'/α" nanodomains[4], but the β → athermal ω transformation in Ti-Nb binary alloys has an energy barrier and thus is a first-order transition[32]. Experimental results have also demonstrated that a thermal hysteresis of ~3 K exists in the β ↔ athermal ω, but no temperature hysteresis can be detected in the transformation of β ↔ O'/α" nanodomains[17]. Therefore, it is different in the transformation path for the formation of athermal ω and O'/α" nanodomains upon cooling.

Moreover, the required initial Nb concentration of the β matrix is different for the transformations to athermal ω and O'/α" nanodomains. A wider concentration range of ≥ 21 at.% Nb has been found in the β → athermal ω[16], whereas the β → O'/α" nanodomains need a higher Nb content of ≥ 25 at.% in the Ti-Nb binary alloys having concentration modulation generated by spinodal decomposition[4]. The shape of athermal ω in the Ti-(21~27) at.% Nb alloys seems concentration-insensitive and shows ellipsoidal nanodomains[5,16], but that of the α" changes from plates in Ti-(15~24) at.% Nb alloys into spherical nanodomains in Ti-(≥ 25) at.% Nb alloys[4]. The APT analysis in solution-treated Ti-23Nb-2O (at.%) alloy has shown that the athermal ω has lower Nb content than the O' nanodomains[14]. The above discussion indicates a relatively weak effect of concentration fields on the formation of athermal ω nanodomains in Ti-Nb alloys with lower Nb content, but the concentration modulation is necessary for the formation of O'/α" nanodomains in Ti-Nb alloys with higher Nb content. As for the metastable phases formed during isothermal aging, we found that the isothermal ω has better phase stability than the O' and α" phases. Previous studies presented the only isothermal ω in Ti-(20-26) at.% Nb alloys after aging at 573 K and 673 K[5,19], and oxygen doping or alloying could increase the phase stability of O' and α" during aging[14,23]. In our current simulations, the competition among the ω, O', and α" is ignored and needs to be further studied.

CONCLUSIONS

A 2D phase field model is developed by coupling the thermodynamic database to simulate the microstructural evolution during the athermal and isothermal β → ω phase transformations for Ti-Nb binary alloys. The simulation results demonstrate that the athermal ω formation is a diffusionless structural transition, and the isothermal ω transformation mechanisms show temperature dependence. The phase transformation also shows concentration dependence. For Ti-50 at.% Nb, concentration modulations are preferentially generated by spinodal decomposition upon water quenching and isothermal aging, in which amplitude and wavelength are tailored by aging temperatures and times. Then, athermal ω and isothermal ω particles nucleate at the Nb-lean β_1 regions, which shape and size could be regulated by the morphological patterns of the precursory composition modulations. Congruent structural transformation followed by decomposition can also be found in aged Ti-50 at.% Nb at 573 K, while isothermal ω particles nucleate at the β_1 regions via pseudospinodal by thermal fluctuations of concentration and structure at 673 K. The differences between transformation mechanisms at different aging temperatures and alloy compositions are the variation origin of the isothermal ω precipitation kinetics.

DECLARATIONS

Authors' contributions

Designed the study and performed data analysis: Su Y
Provided professional guidance: Liang C, Wang D

Availability of data and materials

Not applicable.

Financial support and sponsorship

This work is supported by the National Key Research and Development Program of China (Grand No. 2021YFB3702603), the National Natural Science Foundation of China (Grants No. 51931004 and 52171012), the Fundamental Research Funds for the Central Universities (xhj0320211015-06), 111 Project (BP2018008), the GHfund A (20230219461), and "H2" High Performance Cluster.

Conflicts of interest

All authors declared that there are no conflicts of interest.

Ethical approval and consent to participate

Not applicable.

Consent for publication

Not applicable.

REFERENCES

1. Chou K, Li N, Marquis EA. Enhanced work hardening from oxygen-stabilized ω precipitates in an aged metastable β Ti-Nb alloy. *Acta Mater* 2021;220:117302. DOI
2. Liang Q, Wang D, Zheng Y, et al. Shuffle-nanodomain regulated strain glass transition in Ti-24Nb-4Zr-8Sn alloy. *Acta Mater* 2020;186:415-24. DOI
3. Li T, Wang S, Fan W, et al. CALPHAD-aided design for superior thermal stability and mechanical behavior in a TiZrHfNb refractory high-entropy alloy. *Acta Mater* 2023;246:118728. DOI
4. Su Y, Liang C, Sun X, et al. Composition-dependent shuffle-shear coupling and shuffle-regulated strain glass transition in compositionally modulated Ti-Nb alloys. *Acta Mater* 2023;246:118697. DOI
5. Kim H, Ikehara Y, Kim J, Hosoda H, Miyazaki S. Martensitic transformation, shape memory effect and superelasticity of Ti-Nb binary alloys. *Acta Mater* 2006;54:2419-29. DOI
6. Liang Q, Zheng Y, Wang D, et al. Nano-scale structural non-uniformities in gum like Ti-24Nb-4Zr-8Sn metastable β-Ti alloy. *Scr Mater* 2019;158:95-9. DOI
7. Zhang J, Li Y, Li W. Metastable phase diagram on heating in quenched Ti-Nb high-temperature shape memory alloys. *J Mater Sci* 2021;56:11456-68. DOI
8. Xiong C, Li Y, Zhang J, et al. Superelasticity over a wide temperature range in metastable β-Ti shape memory alloys. *J Alloys Compd* 2021;853:157090. DOI
9. Pang E, Hildyard E, Connor L, Pickering E, Jones N. The effect of quench rate on the β-α″ martensitic transformation in Ti-Nb alloys. *Mater Sci Eng A* 2021;817:141240. DOI
10. Wang K, Wu D, Wang D, et al. Influence of cooling rate on ω phase precipitation and deformation mechanism of a novel metastable β titanium alloy. *Mater Sci Eng A* 2022;829:142151. DOI
11. dos Santos L, Campo KN, Caram R, Najar Lopes ÉS. Oxygen addition in biomedical Ti-Nb alloys with low Nb contents: effect on the microstructure and mechanical properties. *Mater Sci Eng A* 2021;823:141750. DOI
12. Preisler D, Janovská M, Seiner H, et al. High-throughput characterization of elastic moduli of Ti-Nb-Zr-O biomedical alloys fabricated by field-assisted sintering technique. *J Alloys Compd* 2023;932:167656. DOI
13. Lai M, Li T, Yan F, Li J, Raabe D. Revisiting ω phase embrittlement in metastable β titanium alloys: role of elemental partitioning. *Scr Mater* 2021;193:38-42. DOI
14. Li T, Lai M, Kostka A, et al. Composition of the nanosized orthorhombic O′ phase and its direct transformation to fine α during ageing in metastable β-Ti alloys. *Scr Mater* 2019;170:183-8. DOI
15. Li X, Zhao Q, Tian Y, et al. Phase transformation induced transitional twin boundary in body-centered cubic metals. *Acta Mater* 2023;249:118815. DOI
16. Ahmed T, Rack HJ. Martensitic transformations in Ti-(16-26 at%) Nb alloys. *J Mater Sci* 1996;31:4267-76. DOI
17. Todai M, Fukuda T, Kakeshita T. Relation between negative temperature coefficient in electrical resistivity and athermal ω phase in

Ti-xNb (26≤*x*≤29at.%) alloys. *J Alloys Compds* 2013;577:S431-4. DOI
18. Nag S, Devaraj A, Srinivasan R, et al. Novel mixed-mode phase transition involving a composition-dependent displacive component. *Phys Rev Lett* 2011;106:245701. DOI
19. Chou K, Marquis EA. Oxygen effects on ω and α phase transformations in a metastable β Ti-Nb alloy. *Acta Mater* 2019;181:367-76. DOI
20. Ma S, Chen Q, Zhang W, Wang S. The properties of typical β/ω and β/α″ heterophase interfaces in β-Ti alloys from a first-principles insight. *J Mater Sci* 2022;57:4625-42. DOI
21. Qi L, Chen C, Duan H, et al. Reversible displacive transformation with continuous transition interface in a metastable β titanium alloy. *Acta Mater* 2019;174:217-26. DOI
22. Chen W, Cao S, Kou W, et al. Origin of the ductile-to-brittle transition of metastable β-titanium alloys: self-hardening of ω-precipitates. *Acta Mater* 2019;170:187-204. DOI
23. Qi L, He S, Chen C, et al. Diffusional-displacive transformation in a metastable β titanium alloy and its strengthening effect. *Acta Mater* 2020;195:151-62. DOI
24. Wang W, Gong D, Wang H, et al. Spinodal decomposition coupled with a continuous crystal ordering in a titanium alloy. *Acta Mater* 2022;233:117969. DOI
25. Okamoto NL, Kasatani S, Luckabauer M, Enzinger R, Ichitsubo T. Evolution of microstructure and variations in mechanical properties accompanied with diffusionless isothermal ω transformation in β -titanium alloys. *Phys Rev Mater* 2020;4:123603. DOI
26. Li T, Kent D, Sha G, et al. New insights into the phase transformations to isothermal ω and ω-assisted α in near β-Ti alloys. *Acta Mater* 2016;106:353-66. DOI
27. Moffat DL, Kattner UR. The stable and metastable Ti-Nb phase diagrams. *Metall Trans A* 1988;19:2389-97. DOI
28. Thoemmes A, Bataev I, Lazurenko D, et al. Microstructure and lattice parameters of suction-cast Ti-Nb alloys in a wide range of Nb concentrations. *Mater Sci Eng A* 2021;818:141378. DOI
29. Boyne A, Wang D, Shi R, et al. Pseudospinodal mechanism for fine α/β microstructures in β-Ti alloys. *Acta Mater* 2014;64:188-97. DOI
30. Cahn JW, Hilliard JE. Free energy of a nonuniform system. I. Interfacial free energy. *Chem Phys* 1958;28:258-67. DOI
31. Kostorz G. *Theory of structural transformations in solids* by A. G. Khachaturyan. *Acta Crystallogr A Found Crystallogr* 1985;41:208-208. DOI
32. Lai M, Tasan C, Zhang J, Grabowski B, Huang L, Raabe D. Origin of shear induced β to ω transition in Ti-Nb-based alloys. *Acta Mater* 2015;92:55-63. DOI
33. Zhao Q, Sun Q, Xin S, et al. High-strength titanium alloys for aerospace engineering applications: A review on melting-forging process. *Mater Sci Eng A* 2022;845:143260. DOI
34. Ballor J, Li T, Prima F, Boehlert CJ, Devaraj A. A review of the metastable omega phase in beta titanium alloys: the phase transformation mechanisms and its effect on mechanical properties. *Int Mater Rev* 2023;68:26-45. DOI
35. Zhang Y, Xiang S, Tan Y, Ji X. Study on ω-assisted α nucleation behavior of metastable β-Ti alloys from phase transformation mechanism. *J Alloys Compd* 2022;890:161686. DOI
36. Allen SM, Cahn JW. A microscopic theory for antiphase boundary motion and its application to antiphase domain coarsening. *Acta Metall* 1979;27:1085-95. DOI
37. Liu Y, Pan T, Zhang L, Yu D, Ge Y. Kinetic modeling of diffusion mobilities in bcc Ti-Nb alloys. *J Alloys Compd* 2009;476:429-35. DOI
38. Zhu J, Wu H, Wu Y, et al. Influence of Ni_4Ti_3 precipitation on martensitic transformations in NiTi shape memory alloy: R phase transformation. *Acta Mater* 2021;207:116665. DOI
39. Shen C, Simmons J, Wang Y. Effect of elastic interaction on nucleation: II. Implementation of strain energy of nucleus formation in the phase field method. *Acta Mater* 2007;55:1457-66. DOI
40. Zhang T, Wang D, Wang Y. Novel transformation pathway and heterogeneous precipitate microstructure in Ti-alloys. *Acta Mater* 2020;196:409-17. DOI
41. Wang Y, Banerjee D, Su C, Khachaturyan A. Field kinetic model and computer simulation of precipitation of L12 ordered intermetallics from f.c.c. solid solution. *Acta Mater* 1998;46:2983-3001. DOI
42. Choudhuri D, Zheng Y, Alam T, et al. Coupled experimental and computational investigation of omega phase evolution in a high misfit titanium-vanadium alloy. *Acta Mater* 2017;130:215-28. DOI
43. Shi R, Gao Y, Li D, Zhao W, Zheng Y. Recent advances in the design of novel β-titanium alloys using integrated theory, computer simulation, and advanced characterization. *Adv Eng Mater* 2021;23:2100152. DOI
44. Dong T, Liang C, Su Y, et al. Phase field simulations for the crossover from sharp martensitic transformation into smooth strain glass transition by fine precipitates. *Acta Mater* 2023;245:118634. DOI
45. Sharma A, Soni V, Dasari S, et al. Fine scale alpha precipitation in Ti-19at.%v in the absence of influence from omega precipitates. *Scri Mater* 2021;196:113766. DOI
46. An Z, Mao S, Yang T, et al. Spinodal-modulated solid solution delivers a strong and ductile refractory high-entropy alloy. *Mater Horiz* 2021;8:948-55. DOI
47. Xiang T, Zhao M, Du P, Xie G. Heat treatment effects on microstructure and mechanical properties of TiZrNbTa high-entropy alloy. *J Alloys Compd* 2023;930:167408. DOI

48. Radlinger T, Winkler R, Knoll P, et al. A study on the correlation between micro and magnetic domain structure of $Cu_{52}Ni_{34}Fe_{14}$ spinodal alloys. *J Alloys Compd* 2022;922:166214. DOI
49. Chen Y, Yang B, Zhou Y, Wu Y, Zhu H. Evaluation of pitting corrosion in duplex stainless steel Fe20Cr9Ni for nuclear power application. *Acta Mater* 2020;197:172-83. DOI
50. Yao T, Sen A, Wagner A, et al. Understanding spinodal and binodal phase transformations in U-50Zr. *Materialia* 2021;16:101092. DOI
51. Rao Z, Dutta B, Körmann F, et al. Beyond solid solution high-entropy alloys: tailoring magnetic properties via spinodal decomposition. *Adv Funct Mater* 2021;31:2007668. DOI
52. Wu Y, Zhang F, Li F, et al. Local chemical fluctuation mediated ultra-sluggish martensitic transformation in high-entropy intermetallics. *Mater Horiz* 2022;9:804-14. DOI
53. Ishiguro Y, Tsukada Y, Koyama T. Phase-field study of the spinodal decomposition rate of β phase in oxygen-added Ti-Nb alloys. *Comput Maters Sci* 2020;174:109471. DOI